2023

Dissolution-driven propulsion of floating solids

Martin Chaigne

Michael Berhanu

Arshad Kudrolli

PNAS RESEARCH ARTICLE | APPLIED PHYSICAL SCIENCES

Dissolution-driven propulsion of floating solids

Martin Chaigne[a,1], Michael Berhanu[a,1,2], and Arshad Kudrolli[b,1,2]

Edited by Tsvi Tlusty, Institute for Basic Science, Ulsan, Korea (South); received February 3, 2023; accepted June 23, 2023, by Editorial Board Member Mehran Kardar

We show that unconstrained asymmetric dissolving solids floating in a fluid can move rectilinearly as a result of attached density currents which occur along their inclined surfaces. Solids in the form of boats composed of centimeter-scale sugar and salt slabs attached to a buoy are observed to move rapidly in water with speeds up to 5 mm/s determined by the inclination angle and orientation of the dissolving surfaces. While symmetric boats drift slowly, asymmetric boats are observed to accelerate rapidly along a line before reaching a terminal velocity when their drag matches the thrust generated by dissolution. By visualizing the flow around the body, we show that the boat velocity is always directed opposite to the horizontal component of the density current. We derive the thrust acting on the body from its measured kinematics and show that the propulsion mechanism is consistent with the unbalanced momentum generated by the attached density current. We obtain an analytical formula for the body speed depending on geometry and material properties and show that it captures the observed trends reasonably. Our analysis shows that the gravity current sets the scale of the body speed consistent with our observations, and we estimate that speeds can grow slowly as the cube root of the length of the inclined dissolving surface. The dynamics of dissolving solids demonstrated here applies equally well to solids undergoing phase change and may enhance the drift of melting icebergs, besides unraveling a primal strategy by which to achieve locomotion in active matter.

fluid mechanics | self-propulsion | dissolution | natural convection | fluid–structure interaction

Significance

Gravity-driven turbulent flows are well known to occur because of solute concentration gradients, but the fact that an untethered dissolving body can translate robustly as a reaction to such flows has not been demonstrated. By constructing sugar and salt boats, we show that an inclined floating body can self-propel rapidly as it dissolves. The velocities achieved with such flows can be at least an order of magnitude faster compared with those with laminar flows, and thus, our results broaden the conditions under which natural convection can give rise to translation motion of immersed bodies. This propulsion mechanism can apply equally to melting or freezing solids and represents an elemental mechanism by which matter can move actively.

Self-propulsion by converting stored energy into mechanical motion is at the heart of active matter (1). The motion may occur through a chemical reaction enabling ciliary beating in microswimmers (2–4) or by generating ballistic motion at molecular scales by catalytic boosts of enzymes (5). At the granular scale, directed motion can be observed on vibrating substrates via spontaneous symmetry breaking (6) or more robustly with polar grains (7). Self-propulsion can also be created without mechanical action. For example, asymmetric particles which catalyze a chemical reaction in the fluid can break mechanical equilibrium (8). Chemical or temperature gradients can also induce variations of the surface tension on droplets generating propulsion due to the Marangoni effect (9–12), and Leidenfrost droplets can experience propulsion caused by interactions with the substrate (13–15).

Density currents resulting from spatial variations in fluid density constitute another possible mechanism for self-propulsion. This mechanism, which is not restricted to a free surface as in the Marangoni effect and is not limited to microscopic scales, has received limited attention. Passive asymmetric solids floating in density-stratified fluids have been reported to experience thrust, leading them to move slowly with speeds of a few microns per second (16). Faster transport can occur if the body itself generates density variation in the surrounding fluid as demonstrated by Mercier et al. (17) with a floating asymmetric solid with an embedded local heat source that generates thermal convection. However, convective flow can also occur without an added heat source through the progressive phase change of a solid immersed in a fluid. Gravity currents due to solute concentration gradients have been studied to understand shapes changes in dissolving solids (18–22), but whether these flows lead to self-propulsion of the solid itself was unprobed. While autorotation of floating ice disks caused by melting has been noted (23), net translation was not noted in these studies. More recently, dissolving colloidal particles driven by Brownian motion have been considered theoretically and predicted to undergo stochastic dynamics (24), but any effect of convective flow of the surrounding fluid as a result of the dissolution was not examined.

Here, we show that an unconstrained asymmetric dissolving solid can propel itself rectilinearly because of the thrust generated as a reaction to the unbalanced momentum of the solute-rich density current which develops along its inclined surfaces. While we focus here on the case of dissolution because it does not have the complexity associated

Author affiliations: [a]Laboratoire Matière et Systèmes Complexes, Université Paris Cité, CNRS (UMR 7057), F-75013 Paris, France; and [b]Department of Physics, Clark University, Worcester, MA 01610

Author contributions: M.C., M.B., and A.K. designed research; performed research; analyzed data; and wrote the paper.

The authors declare no competing interest.

This article is a PNAS Direct Submission. T.T. is a guest editor invited by the Editorial Board.

[1]To whom correspondence may be addressed. Email: martin.chaigne@u-paris.fr, michael.berhanu@u-paris.fr, or akudrolli@clarku.edu.

[2]M.B. and A.K. contributed equally to this work.

This article contains supporting information online at https://www.pnas.org/lookup/suppl/doi:10.1073/pnas.2301947120/-/DCSupplemental.

Published July 31, 2023.

with temperature gradients and phase change, the elucidated propulsion mechanism applies equally well to asymmetric bodies undergoing melting. We further discuss the implication for active transport of floating ice as a result of melting or freezing, relative to their advection due to wind and ocean currents (25–28).

1. Results

A. Design and Observations. We construct dissolving bodies in the form of boats which float asymmetrically in water by attaching a solid 7.5 cm × 4.0 cm × 0.5 cm rectangular candy slab to the bottom of a hollow plastic box which acts as a buoy. A schematic of such a candy boat is shown in the *Inset* to Fig. 1*A*, and further details on its fabrication process can be found in the *Methods*. When the composite boat floats in water, the placement of the buoy relative to the center of the heavier candy slab determines the inclination angle θ of the dissolving surfaces as shown in Fig. 1*B*. In all, a set of 9 boats with mass m of approximately 33 g each were constructed with identical dissolving slabs and buoys to vary θ between 0° and 80° and to study the effect of breaking fore–aft symmetry on their dynamics.

Fig. 1*A* and Movie S1 show a time sequence of a dissolving solid boat corresponding to $\theta = 22°$ moving in fresh water after it is released from rest in a large tank. We observe from the superimposed trajectory of the candy boat that it moves essentially rectilinearly while achieving speeds of order 5 mm/s. By contrast, we observe that the boat drifts slowly with speeds less than 0.7 mm/s if the plastic hull is placed centrally, which results in $\theta \approx 2°$ (Movie S2). Thus, symmetry breaking due to the inclination of the dissolving body is important to the observed rapid rectilinear motion.

We further visualize the solvent bath to examine the solute-rich fluid which occurs around the dissolving body. The images shown in Fig. 1*B* and Movie S3 are taken with the shadowgraph technique which magnifies refractive index variations caused by the solute concentration. Turbulent plumes are observed to emerge directed behind and below the dissolving surface as the boat moves forward, but the area near the air–water interface around the boat does not show any refraction due to the presence of solute which may signal surface tension gradients. We further visualize the fluid motion with Particle Image Velocimetry (PIV) by adding fluorescent tracers as discussed in *SI Appendix*, section 1. PIV measurements. Fig. 1*C* shows the corresponding flow field v_f obtained with PIV in a vertical cross-sectional plane. To our knowledge, the convection flow below a dissolving body has not been quantitatively characterized previously. The fluid can be observed to accelerate rapidly below the inclined dissolving surface before detaching and flowing downward with the greatest velocities directed below and behind the dissolving surface. Because the solute-rich fluid descends rapidly to the bottom of the tank, the fluid near the surface remains solute-free since the fluid is drawn in apparently faster than the time scale over which the solute can diffuse out around the dissolving solid. Thus, the boat is seen to move opposite to the direction of the density current which flows toward the back, while moving down due to the action of gravity.

By adding weights to the plastic box, we submerged the entire body to a depth of 4 cm, turning it into a submarine. To maintain a constant immersion depth, a stratified bath was prepared with a fresh water layer lying over a denser salt water layer (for more details, see *SI Appendix*, section 2). We observe that the boat moves similarly as shown in Movie S4 with speeds up to 1 mm/s,

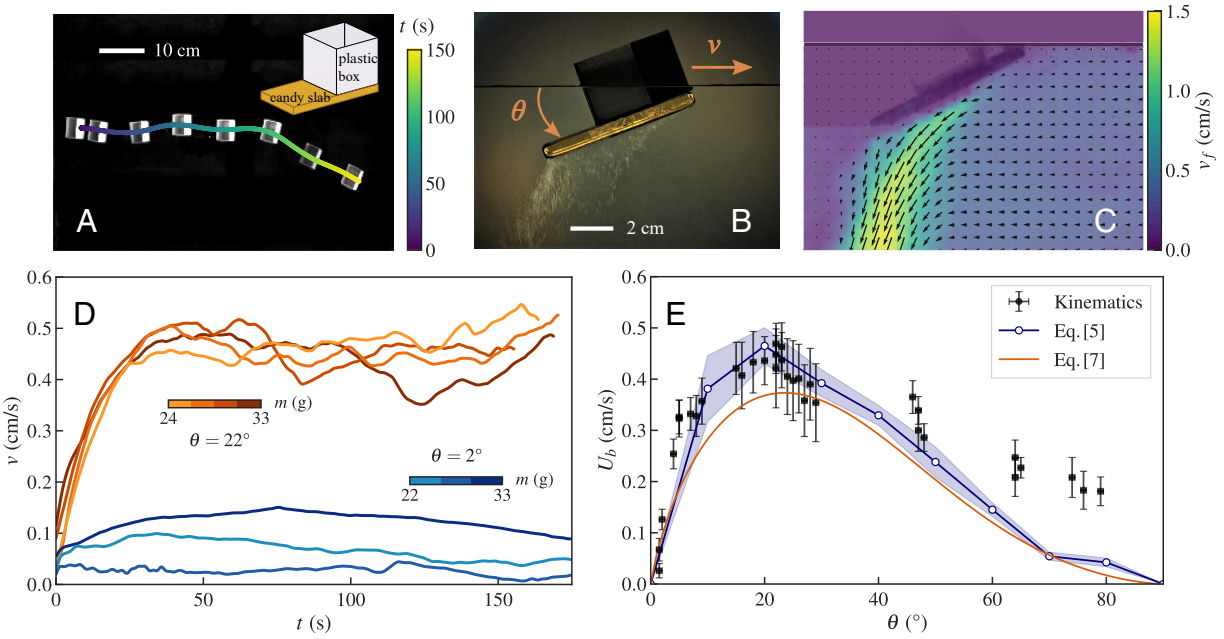

Fig. 1. Kinematics of the candy boats. (*A*) Superimposed images at 20-s time intervals show the motion of a candy boat in a large tank of water (top view). (*Inset*) Schematic of a candy boat. (*B*) An image of a candy boat moving in water obtained with shadowgraph technique (side view). Solute-rich plumes are visible descending below the dissolving boat. (*C*) The fluid velocity v_f in the body frame of reference measured with PIV in the mid-vertical cross-section of the boat superimposed on an image of the system ($\theta = 26° \pm 1°$). The magnitude and direction of v_f averaged over 15 s are shown with arrows and color map. (*D*) The evolution of boat velocity v corresponding to consecutive launches with two different boats: $\theta = 22° \pm 1°$ (orange lines) and $\theta = 2° \pm 1°$ (blue lines). The mass m decreases with each trial and is shown by a color bar for each boat. (*E*) The measured boat speed U_b (•) varies significantly with θ and is well described by estimates obtained by performing a momentum balance analysis (Eq. **5**) with measured flow fields in Section 2, and by the functional analysis which leads to Eq. **7** combined with Eq. **8** in Section 3. The blue shade corresponds to the estimated error in determining F_p^{MB}. Systematic deviations are observed at higher θ because only the contribution of the flow below the dissolving slab is considered for simplicity of analysis.

roughly the same order of magnitude as when floating at the air–water interface. This observation further confirms that the propulsion mechanism at play is different from Marangoni flows which can propel dissolving solids such as camphor boats due to surface tension gradients (29–31).

We also performed measurements with dissolving boats where the sucrose block was replaced with a salt (NaCl) block with dimensions 4.1 cm × 2.3 cm × 0.6 cm to test whether the propulsion can be observed with other dissolving materials. The same qualitative behavior is observed with $U_b \approx 4.2$ mm/s when $\theta = 40°$ (*SI Appendix*, section 3). Unlike sugar–water solutions where viscosity can vary several orders of magnitude when the saturation limit is reached, the viscosity of saturated salt solution is only higher by a factor 2 compared with water (32). Thus, the large viscosity variations specific to sugar solutions do not play an appreciable role in the propulsion.

To further check the robustness of the propulsion mechanism, and its persistence in multibody environments, we performed experiments with two candy boats with the same length $L = 7.5$ cm, and $\theta = 33° \pm 2°$. As shown in Movie S5, when the boats are moving in a row in the same direction, the following boat catches up with the leading boat, and the boats self-assemble to move forward in tandem. While approaching from opposite directions, the boats come in contact, pair up, and then spin around each other as shown in Movies S6 and S7, with speeds that depend on their relative contact position (*SI Appendix*, section 4). Thus, we find that while capillary interactions, important over the scale of a centimeter or less (33, 34), cause these bodies floating at the surface to stay in contact, it is clear that such boats can move collectively and can show further rich phenomena.

B. Kinematics. Fig. 1*D* shows the measured boat velocity v obtained from the displacement of its center of mass position over a time interval of 0.2 s as a function of time t corresponding to $\theta = 22°$. Four consecutive launches of the same boat are shown to illustrate the robust features of the kinematics. We observe that v increases smoothly before the turbulent nature of the plumes, and rudderless nature of the boat causes its velocity to fluctuate somewhat randomly. The total mass of the boat is observed to decrease by approximately 10% over the course of the entire trial. Since θ depends on the relative mass and location of the buoy and the heavier dissolving block, it can evolve slowly over time in principle with dissolution. However, the measured θ was observed to be constant to within 1° in these examples, and no systematic variation from one launch to the next can be observed. We obtain the boat cruising speed $U_b \approx 4.5$ mm/s by averaging over the time after the boat stops accelerating forward (about $t = 40$ s here) and while it maintains a more or less constant speed. These observed speeds are faster by an order of magnitude compared with previous demonstrations of temperature-gradient-driven convective transport in immersed bodies (17) and more than two orders of magnitude faster than diffusion-driven transport in stratified fluids (16).

We investigate U_b further as a function of the inclination of the dissolving surfaces using the nine different candy boats constructed with different buoy locations. Fig. 1*E* shows the mean U_b and θ along with their standard deviations for a given trail. We observe that U_b increases rapidly reaching a peak at $\theta \approx 22°$ before decreasing as θ increases toward 80°. The overall increase and then decrease of speed with θ is consistent with the rectangular geometry of a dissolving block which would be symmetric about the vertical axis, when $\theta = 0°$ and 90°. Thus, the significant dependence of speed on θ highlights the importance of orientation of the dissolving surfaces on the propulsion of the dissolving bodies in our experiments.

C. Thrust and Drag. We examine the forces acting on the floating body as it dissolves, toward understanding its kinematics. Because the identification of distinct portions of the body over which the propulsive and the retarding forces apply is complex, we assume that the force exerted by the fluid on the boat is written as a constant term F_p, which we call "thrust," minus a term increasing with the velocity F_d, which we call "drag." Such a decomposition is widely used, for example, to model the kinematics of swimming bodies in the inertial regime (35–37), when the thrust and the drag result from a pressure field. The boat accelerates due to these unbalanced forces acting on it toward the bow along its symmetry axis. Neglecting the change in mass of the body, the net force $F_{\text{net}} = F_p - F_d$ is proportional to the acceleration of the body according to $F_{\text{net}} = m\,\mathrm{d}v/\mathrm{d}t$, where we ignore the added mass effect which may arise because moving a body requires displacing the fluid in which it is immersed (38–40). We plot $F_{\text{net}} = m\,\mathrm{d}v/\mathrm{d}t$ as a function of time in Fig. 2*A* and observe

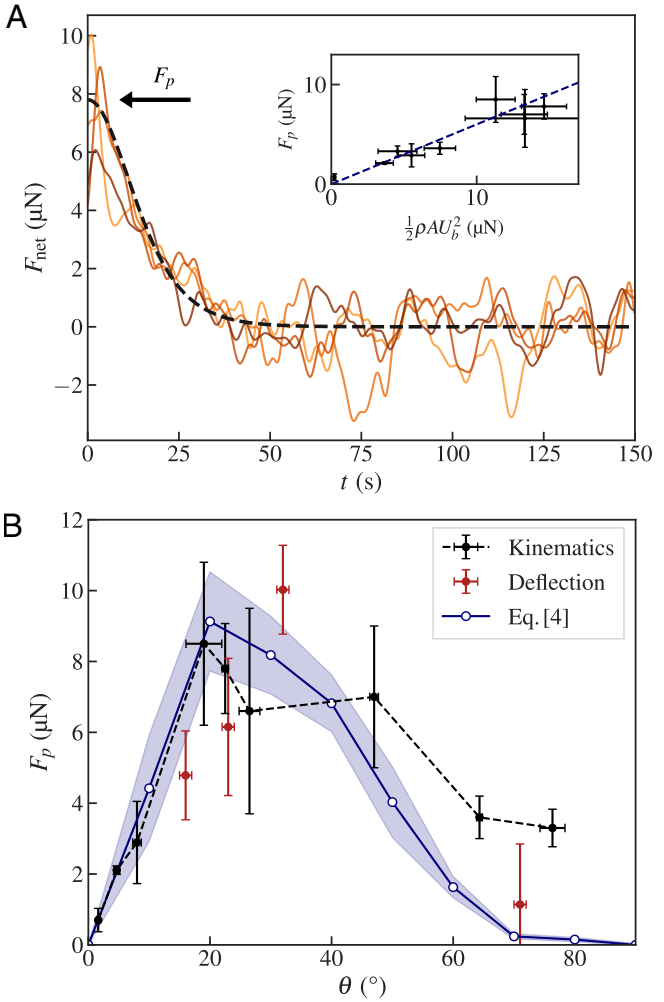

Fig. 2. Forces acting on a moving dissolving body. (*A*) The net force F_{net} decays to zero as the drag increases with speed and balances the thrust F_p. The dashed line corresponds to *SI Appendix*, Eq. **S2** assuming v^2-drag (*SI Appendix*, Text 4). (*Inset*) F_p versus $F_d/C_d = \frac{1}{2}\rho L_A W U_b^2$. The data are described by a linear fit corresponding to quadratic-drag with $C_d = 0.6$. (*B*) The thrust F_p obtained using kinematic measurements, deflection measurements, and calculated using the momentum balance condition given by Eq. **4**, and its estimated error (blue shade).

that it is highest close to $t = 0$ s when $v \approx 0$ mm/s. F_{net} then decreases rapidly toward zero as drag increases and balances the thrust. When $v \to 0$, we have $F_d \to 0$ and $F_{\text{net}} \to F_p$. We plot F_p as a function of θ in Fig. 2*B* and observe that it increases and decreases with θ following the trends in U_b with θ. We performed further complementary measurements of F_p by obstructing the boat's forward motion using a long thin rod and measuring its deflection (Fig. 2*B*). The measured thrusts using the two methods are in overall agreement, confirming that the added mass effect can be neglected at least at low to moderate θ.

If the thrust does not change with v, we have $F_d = F_p$ when the boat moves with speed U_b. The drag can be written in general as $F_d = \frac{1}{2} C_d \rho_f A U_b^2$, where $\rho_f = 997\ \text{g L}^{-1}$ is the density of water, A is the projected area along the direction of the boat's velocity, and C_d is the drag coefficient. We have $A = L_A W$, where W is the width, and L_A is the projected length measured for each boat from a side view image corresponding to the projected length of its immersed part on the vertical axis (*SI Appendix*, section 5). The Reynolds Number over the scale of the boat can be estimated as $Re = U_b L/\nu \approx 340$ since $L = 7.5$ cm, $U_b \approx 4.5$ mm/s, and $\nu = 1.00 \times 10^{-6}\ \text{m}^2\ \text{s}^{-1}$, the kinematic viscosity of water at 20 °C. Since $Re \gg 1$, the drag can be expected to scale quadratically with speed. We plot F_p versus $F_d/C_d = \frac{1}{2}\rho L_A W U_b^2$ in the *Inset* of Fig. 2*A*, where each point represents averaged values over trials of the same boat. The data are observed to be well described by a linear fit, with a slope corresponding to $C_d = 0.6$, which is reasonable considering C_d for a nonstreamlined body (38).

We calculate an analytical expression for F_{net} over time assuming thrust F_p independent of v, and $F_d = \frac{1}{2} C_d \rho A v^2$ in *SI Appendix*, section 6. Plotting F_{net} using the measured ratio $C_d = 0.6$ in Fig. 2*A* (dotted line), we find good agreement with the time scales over which the boat accelerates. This agreement validates our assumption that the thrust generated by the dissolution is essentially independent of the speed of the boat and depends only on the angle of inclination of the dissolving surface. Even though it is not obvious in general, the agreement also confirms a posteriori the decomposition of forces into thrust and drag on the same surface. Thus, we find that a dissolving body released from rest accelerates and reaches a cruising velocity as its drag increases and matches the thrust corresponding to its geometry.

D. Effect of Dissolving Surface Orientation. We gauge the relative effect of the upward- and downward-facing surfaces of the dissolving slab on the propulsion speed by adding a thin plastic wing to the side of the plastic box such that the dissolving slab is covered from above or below. The measured speeds are given in Table 1 corresponding to $\theta = 45°$. While the greatest speed is achieved when both the top and bottom surfaces of the slab are allowed to dissolve, U_b is about five times greater when the bottom surface is exposed compared to the top surface. The presence of the buoy screens part of the slab, resulting in the area of the bottom surface being nearly two times larger than the top surface. Thus, while part of the greater contribution of the bottom surface is due to its larger surface area, bottom-facing surfaces dissolve faster than top-facing surfaces (41).

Table 1. Measured mean speed U_b and its standard deviation corresponding to the exposed dissolving surfaces of the dissolving slab ($\theta = 45°$)

Dissolving surface	Speed U_b (mm/s)	Area (cm^2)	$\dot{h}$ (mm/s)
Bottom and top	3.3 ± 0.2	48	—
Bottom	2.6 ± 0.2	30	2.41×10^{-3}
Top	0.5 ± 0.2	18	0.87×10^{-3}

The difference in surface area and dissolution rate can account for the relative contribution of the bottom and top surfaces on U_b.

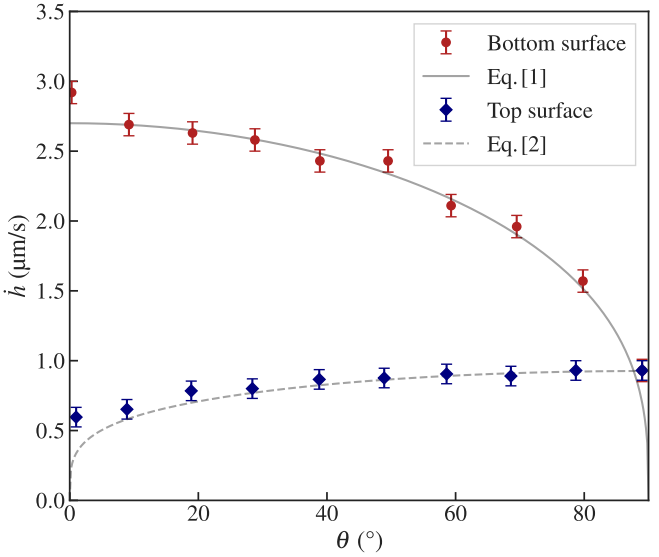

Fig. 3. The measured recession rate $\dot{h}$ along the top and bottom surfaces of the dissolving block as a function of its inclination angle θ. Gray lines: Calculated recession rates at the bottom surface (Eq. **1**, solid line), where a density inversion instability leads to faster $\dot{h}$, with $Ra_c = 1101$ and $\nu_i = 2.5 \times 10^{-4}\text{m}^2\text{s}^{-1}$, and at the top surface (Eq. **2**, dashed line) with fitting parameter $B = 1.15 \times 10^{-4}\text{cm}^{5/4}\text{s}^{-1}$ (42). Greater boat speeds are observed when the bottom surface dissolves compared to the top surface at the same inclination angle.

To ascertain the effect of inclination on the dissolution of the body and its effect on U_b, we measure the location and evolution of the dissolving surface at various θ. Fig. 3 shows the recession rate $\dot{h}$ of the dissolving surface as a function of its orientation. Because of the solutal Rayleigh–Bénard instability, $\dot{h}$ is greatest when $\theta = 0°$, but decreases as θ increases when the dissolving surface faces down.

The recession rate $\dot{h}$ can be calculated based on material properties and the inclination of the dissolving surface. In the presence of solutal convection (41), $\dot{h} = \dfrac{D\,\rho_{sat}\,c_{sat}}{\rho_s\,\delta_c\,(\rho_{sat} - c_{sat})}$, where ρ_s is the density of the dissolving solid, ρ_{sat} is the saturation density of the solute, c_{sat} is the saturation concentration, D is the diffusion coefficient, and δ_c is the concentrated solute boundary layer thickness (*SI Appendix*, section 7). When the surface is oriented downward, the boundary layer is subject to a Rayleigh–Bénard instability. In the quasi-stationary regime, δ_c is set by the critical Rayleigh number Ra_c (18–20). The effect of the inclination can be taken into account by considering the projection of the gravity perpendicular to this layer (21). Then, $\delta_c = \left(\dfrac{Ra_c\,\nu_i\,\rho_f\,D}{g\cos\theta\,(\rho_{sat} - \rho_f)}\right)^{1/3}$, where Ra_c can be approximated as 1101 in case of a Rayleigh–Bénard instability in a layer with mixed slip and nonslip boundary conditions (43), ρ_f is the density of the far field liquid, and ν_i is the average viscosity of the boundary layer. Thus, the recession rate at the bottom surface is

$$\dot{h}_b = \frac{\rho_{sat}\, c_{sat}\, D^{2/3}}{\rho_s\,(\rho_{sat} - c_{sat})} \left(\frac{g \cos\theta\,(\rho_{sat} - \rho_f)}{Ra_c\, \nu_i\, \rho_f} \right)^{1/3}. \quad [1]$$

We evaluate $\dot{h}_b$ using the parameters corresponding to sucrose dissolving in fresh water, where ρ_s = 1,430 g L^{-1}, ρ_f = 997 g L^{-1}, ρ_{sat} =1,300 g L^{-1}, c_{sat} = 940 g L^{-1}, $D = 4.3 \times 10^{-10}$ m^2 s^{-1}, and $\nu_i = 2.5 \times 10^{-4}$m^{2}s^{-1} by interpolating between the saturation concentration $\nu_s = 7.7 \times 10^{-4}$m^{2}s^{-1} and the fresh water $\nu = 1.0 \times 10^{-6}$m^{2}s^{-1} (19, 41). A comparison is plotted in Fig. 3, and good agreement is observed.

At the top surface of the slab, the convection is gravitationally stable, and one can obtain (*SI Appendix*, section 7) an expression for dissolution rate averaged over the length of the dissolving surface as

$$\dot{h}_t = \frac{4B \sin\theta^{1/4}}{3L^{1/4}}, \quad [2]$$

where B is a material-dependent fitting parameter. This expression is also plotted in Fig. 3 and observed to describe the data reasonably, except near $\theta = 0°$, because the expression is valid only for sufficiently inclined surfaces that give rise to a slope-driven buoyancy flow (42).

Thus, the body dissolving asymmetrically with θ with density inversion instability leads to faster dissolution at the bottom surface, which in turn leads to faster U_b. At $\theta = 45°$, $\dot{h}$ is approximately 2.5 times higher at the bottom surface compared to the top surface. This factor along with the difference in surface area partly explains the nearly five times higher speeds recorded when the bottom versus top surfaces alone are allowed to dissolve as noted in Table 1.

2. Propulsion Mechanism

To explain the motion of the dissolving body, we hypothesize that the solute-rich density current creates a pressure difference fore and aft of the immersed body, giving rise to the thrust needed to accelerate the body from rest (the direct thrust due to the dissolution of mass at a rate given by $\dot{h}$ can be calculated to be negligible as shown in *SI Appendix*, section 8). When the dissolving surface is located above the solvent, the solute-rich fluid layer is susceptible to a solutal density inversion instability (41). As seen in the shadowgraph image Fig. 1*B*, the dense fluid does not sink strictly vertically. The gravity-driven current acquires a horizontal component due to a suction effect. Low pressure is created at the bottom face of the slab due to the sinking plumes which causes the boundary layer to remain attached to the surface, while gravity causes it to flow downward. Thus, the flow must have a horizontal component, directed backward relative to the boat. The forward motion of the boat can then be seen in two ways, which are ultimately equivalent, in terms of force or in terms of momentum: either as the result of the net flow directed backward or as the result of the low-pressure region located along the candy slab which induces a net horizontal force. While buoyancy rapidly ensures vertical balance, the solid is pulled horizontally by the low-pressure region in the direction opposite to the horizontal component of the sinking fluid, providing the propulsion mechanism. If the dissolving surface is located below the solvent, the solute-rich fluid follows the inclined surface in a barely visible thin layer due to unbalanced gravitational force when $\theta > 0$ and is ejected off to the sides as it falls over the inclined dissolving slab. Such a flow would give rise to reaction forces which would further contribute to the propulsion of the boat. Since the downward-facing surface dissolves faster and makes a dominant contribution to the observed speed as discussed in Section D, we only focus on the region below the dissolving slab to develop a simplified quantitative understanding of the thrust which accelerates the boat.

A direct evaluation of the pressure field on the solid wall is difficult because of the intermittent nature of the plumes and the complex flow geometry. Therefore, we employ an approach using momentum balance to calculate the thrust from the measured mean velocity field near the dissolving solid. When the boat moves with constant velocity, it is not possible to evaluate thrust using the flow field because the thrust equals drag in that limit. However, the thrust can be evaluated from the flow field around a stationary boat since the thrust remains independent of speed according to Fig. 2*A*. Therefore, we perform a series of measurements of the flow field below an identical dissolving slab held at rest with various θ.

Fig. 4 *A*–*C* shows examples of observed flow fields at low, intermediate, and high inclination angles, respectively, obtained with PIV. We observe that the overall flow is more or less downward along gravity at small θ but becomes increasingly attached to the dissolving surface with increasing θ. The asymmetry of the slab thus leads the flow to acquire a strong lateral component: This, in addition to being an interesting finding in itself, is crucial for propulsion. The main features of the solute-rich fluid flow are schematically represented in Fig. 4*D*, where a steady flow with velocity v_p is directed along the dissolving surface. We denote δ_v the thickness over which the flow velocity decreases to half its value. We estimate v_p from the measurements through the horizontal surface below the dissolving body bounded by the x_1 and x_2 planes and plot it in Fig. 4*E* as a function of θ. We observe that v_p increases rapidly as the inclination of the dissolving slab is increased from $\theta = 0°$ and reaches a peak over a similar range as U_b, before decreasing as the dissolving surface becomes vertical. Further, we plot the projection δ_x of the rapidly flowing layer δ_v on the axis between x_1 and x_2 scaled by L in Fig. 4*F*. δ_x decreases monotonically with θ and is well described by the empirical form:

$$\frac{\delta_x}{L} = \frac{1}{2}\cos^2\theta. \quad [3]$$

It can be noted that $\delta_x = L/2$ when $\theta = 0°$, meaning that the width of the rapid current below a horizontal slab is only half that of the slab. Then, δ_x/L decreases when θ increases since the flow becomes increasingly narrow and attached to the slab.

Hence, we consider the prismatic volume $\mathcal{V}$ below the inclined dissolving surface, as illustrated in Fig. 4*D*, bounded by the dissolving surface, the horizontal plane $z = z_1$, and the vertical planes $x = x_2$, $y = y_1$, and $y = y_2$ with $y_{1,2} = \pm W/2$. Assuming the fluid to be inviscid and incompressible, we obtain the horizontal component of the thrust acting on the dissolving surface considering momentum balance (38) along the horizontal x-axis as

$$\begin{aligned} F_p^{MB} = &- \int_{y_1}^{y_2}\int_{z_1}^{z_2} \rho\, v_x^2\, \mathrm{d}y\, \mathrm{d}z\,|_{x=x_2} \\ &+ \int_{z_1}^{z_2}\int_{x_1}^{x_2} \rho\, v_y\, v_x\, \mathrm{d}x\, \mathrm{d}z\,|_{y=y_1} \\ &- \int_{z_1}^{z_2}\int_{x_1}^{x_2} \rho\, v_y\, v_x\, \mathrm{d}x\, \mathrm{d}z\,|_{y=y_2} \\ &+ \int_{y_1}^{y_2}\int_{x_1}^{x_2} \rho\, v_z\, v_x\, \mathrm{d}y\, \mathrm{d}x\,|_{z=z_1}, \end{aligned} \quad [4]$$

where ρ is the fluid density and v_x, v_y, and v_z are the respective velocity components along the x, y, and z axes as defined in

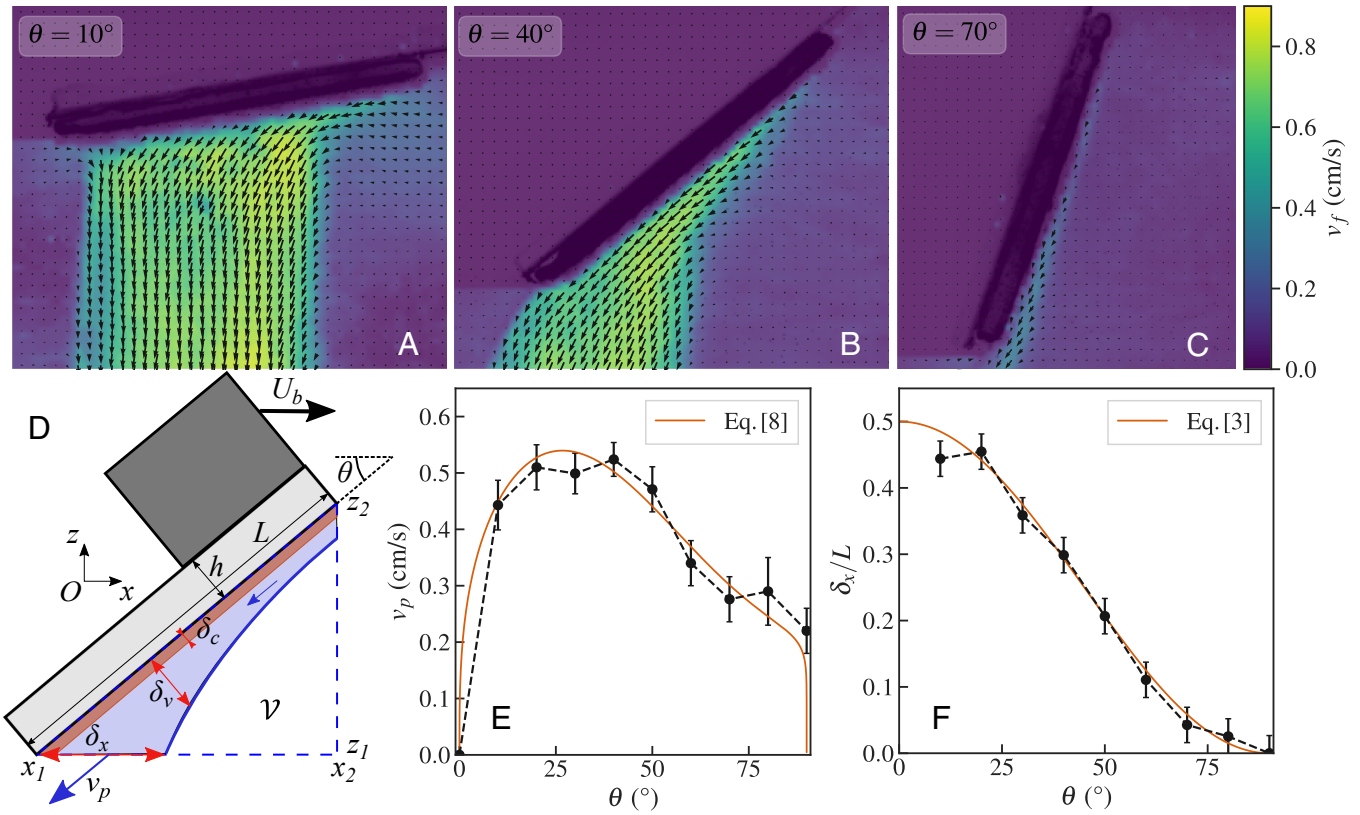

Fig. 4. Buoyancy driven flow characterization. (*A–C*) Velocity field under the static candy plate at three different inclinations. (*D*) A schematic of the main features of the flow in the vertical plane important to determining the thrust on the bottom surface of the dissolving slab. A prismatic volume $\mathcal{V}$, denoted by the blue dashed lines with lateral width W, below the dissolving surface is used in analyzing the momentum balance. The flow leaving $\mathcal{V}$ through the bottom side is mostly confined over a length δ_x and has a magnitude v_p. The rapid flow is confined over a distance δ_v perpendicular to the dissolving surface, and δ_c is the thin nearly saturated solute boundary layer. (*E*) Plot of v_p, corresponding to the maximal value of the parallel component of the fluid velocity at $z = z_1$ between x_1 and x_2, as a function of θ. The solid orange line corresponds to a theoretical estimation according to Eq. **8**, with a dimensionless prefactor of order one depending on the angle chosen to fit the data (*SI Appendix*, section 11 and Fig. S9). (*F*) The effective width of the rapid flow δ_x/L versus θ. The solid orange line corresponds to the empirical formula given by Eq. **3**.

Fig. 4*D*. The terms on the right-hand side correspond to the fluid entering $\mathcal{V}$ through vertical plane $x = x_2$, bounding vertical planes $y = \pm W/2$, and leaving through the bottom horizontal plane $z = z_1$. Because the mass of dissolved solute is negligible compared to the mass of the fluid, we evaluate each term separately assuming that ρ is given by the density of fresh water ρ_f in $\mathcal{V}$ (*SI Appendix*, section 9). We find that the term corresponding to the bottom plane dominates over the entire range of θ (*SI Appendix*, section 10 and Fig. S8). Thus, F_p is positive, in agreement with the direction of the acceleration when the body is released.

We compare the calculated magnitude of F_p^{MB} using Eq. **4** with data as a function of θ in Fig. 2*B*, and we find that it is overall in agreement with the thrust obtained from both the kinematic as well as the deflection measurements. Thus, we conclude that momentum balance gives a reasonable description of the observed thrust needed to accelerate the body from rest as seen in our experiments. While F_p^{MB} underestimates observed F_p obtained from the kinematics, this is to be expected since we neglect the contribution of the top surface to propulsion, which becomes relatively more important as θ increases.

We can further compare the predicted speeds according to momentum balance to those measured in the experiments using the fact that we have $F_p = F_d$ and $F_d = \frac{1}{2} C_d \rho_f A U_b^2$, when the boat moves with constant velocity. Then,

$$U_b^{MB} = \sqrt{\frac{2F_p^{MB}}{C_d\, \rho_f\, A}}\,. \qquad [5]$$

Fig. 1*E* shows U_b^{MB} (blue line) compared with measured U_b corresponding to each trial with the 9 different boats. Good agreement is observed with U_b, except for $\theta > 60°$, where contribution of the attached convection flow on the top of the dissolving slab may become significant. Thus, we find that the mechanism of propulsion based on the pressure variation produced by the attached sinking density current can capture the overall order of magnitude of the thrust acting on the dissolving body and the speeds attained as a function of the inclination angle.

3. Functional Analysis of Boat Speed

In order to understand the physical and geometrical parameters setting the boat velocity U_b beyond the propulsion mechanism, we further simplify the flow modeling. We consider only the term corresponding to the flow through the bottom surface $z = z_1$ in Eq. **4** since it makes the dominant contribution to determine F_p (*SI Appendix*, Fig. S8). Further, measurements taken in the $y - z$ plane (*SI Appendix*, section 1) show that the descending density flow is mainly confined to the central half width of the dissolving surface. The flow out of z_1 is thus mostly confined over a region

with length scale δ_x and width $W/2$, with an approximate flow velocity $v_x = v_p \cos\theta$ and $v_z = v_p \sin\theta$, and we have

$$F_p^{MB} \approx \rho_f \frac{W}{2} \delta_x v_p^2 \sin\theta \cos\theta . \quad [6]$$

Then, using Eq. **5** and $A = L_A W$ (Section C), we have

$$U_b^{th} = \sqrt{\frac{\sin 2\theta \, \delta_x}{2 C_d L_A}} v_p . \quad [7]$$

Thus, we observe that the body speed is set by v_p besides other geometric factors related to the size and asymmetry of the floating body. Using Eq. **3** to express δ_x and *SI Appendix*, Eq. **S1** to capture the measured dependency of the projected length L_A (*SI Appendix*, section 5), we find that $\sin 2\theta \, \delta_x/L_A$ has a maximum at $\theta \approx 21°$, which equals 0.58. Thus, we then find that U_b^{th} is of a similar order of magnitude as v_p at $\theta \approx 20°$ from Eq. **7** since $C_d \approx 0.6$. This analysis which shows that the boat speed is of similar order of magnitude as the density current speed is consistent with our observations in Figs. 1*E* and 4*E* at intermediate θ.

We can estimate v_p itself by balancing the pressure difference which gives rise to the rapid flow below the dissolving slab, starting from (x_2, z_2) and ending at (x_1, z_1), due to the nonbuoyant weight of the solute-rich fluid with the drag as a result of inertial friction exerted by the quiescent fluid below and the dissolving surface above. Assuming that the shear occurs over length scale δ_v, we have $\Delta\rho \, g \, L \sin\theta = f_D \, \rho_f \frac{L}{\delta_v} v_p^2$, where $\Delta\rho$ is the increase in density due to the dissolved solute and f_D is a dimensionless friction factor (38, 44). Using mass conservation of the solute, we have $\Delta\rho = \frac{\rho_s \dot{h} L}{\delta_v v_p}$, where ρ_s is the density of the dissolving solid and $\dot{h}$ is the recession rate of the dissolving surface given by Eq. **1**. Thus,

$$v_p = \mu_p \left(\frac{\rho_s \, g \, L \sin\theta \, \dot{h}}{\rho_f} \right)^{1/3} , \quad [8]$$

where $\mu_p = 1/f_D^{1/3}$. Plugging in the values corresponding to where the maximum speed is observed ($\theta = 22°$) in $v_p^o = \left(\frac{\rho_s \, g \, L \sin\theta \, \dot{h}}{\rho_f} \right)^{1/3}$, we find that it is 10.1 mm/s, comparable in magnitude to the measured $v_p = 5.1$ mm/s. Thus, μ_p is a parameter which is of order 1. Because the geometry of the flow evolves with θ, μ_p is not constant. Thus, we plot the ratio v_p/v_p^o in *SI Appendix*, Fig. S9 and find its dependence on θ. We plot Eq. **8** with the empirical value of μ_p as a function of θ in Fig. 4*E*. Hence, we can estimate the value of U_b^{th} using Eq. **8** and the empirical forms for δ_x/L and L_A as a function of θ. We plot U_b^{th} versus θ in Fig. 1*E* (orange line) and observe that the estimated values follow the same trends as the data especially over low and intermediate inclination angles. U_b^{th} can be observed to be systematically increasingly lower with increasing θ. This trend is consistent with the expectation that the flow near the top surface becomes increasingly important as θ increases toward 90°, although other assumptions in our model may contribute to these systematic deviations as well.

To test the robustness of the measurements and derived dependence further, we built additional boats with L between 7.5 cm and 2.6 cm. The data corresponding to each measured trail with the candy boats with various L are plotted in Fig. 5*A* versus the measured θ. Comparing U_b at similar θ, we note that speeds are lower for smaller L. To understand whether this is consistent with our analysis, we combine Eqs. **3**, **7**, and **8**, and the general expression of the erosion rate to obtain the following scaling after neglecting θ-dependence,

$$U_b^{th} \approx (Dg)^{1/3} \left(\frac{c_{sat} \, \rho_{sat}}{\rho_f \, (\rho_{sat} - c_{sat})} \right)^{1/3} \delta_c^{-1/3} L_A^{-1/2} L^{5/6} . \quad [9]$$

The first term constitutes the intrinsic velocity scale of the system and interestingly gives the right order of magnitude for the boat speed; i.e., $(Dg)^{1/3}$ is of the order of 1.6 mm/s for sugar in water and 2.5 mm/s for salt. Then, we can expect the explicit length dependence to scale as $L^{5/6} L_A^{-1/2}$, which reduces to $L^{1/3}$ when $L_A \approx L$ (*SI Appendix*, section 12). Accordingly, we plot $U_b L^{-5/6} L_A^{1/2}$ versus θ in Fig. 5*B* and find that the data collapse onto a common curve, showing that the length dependence is captured by our analysis. Here again, as in Fig. 1*E*, we observe

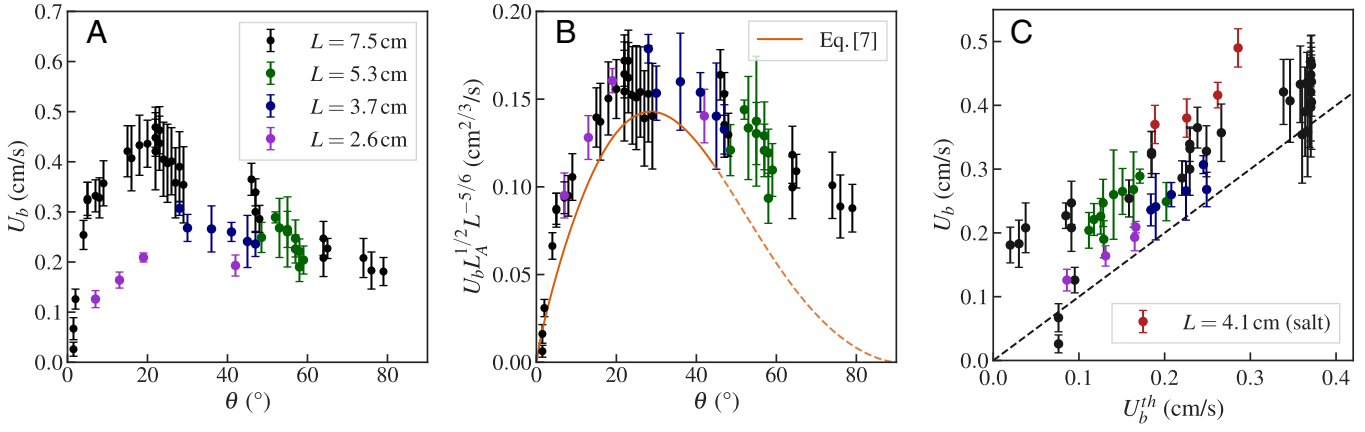

Fig. 5. Boat velocity for various sizes and comparison with the model. (*A*) Measured U_b corresponding to candy boats with various sizes as a function of θ. (*B*) The data from the various boats collapse after scaling with L and L_A. Eq. **7** (solid orange line) matches the data at a 10% level for $\theta < 45°$ but underestimates the data for higher θ (dashed orange line) because contributions of flows above the dissolving slab are not taken into account. (*C*) Comparison of measured U_b and U_b^{th} (Eq. **7**) corresponding to various candy and salt boats of various sizes. The trends are in overall agreement, with measured values being systematically higher compared to calculated values which only consider the contributions of flow below the boat in calculating the thrust.

that the theoretical curve given by Eq. **7** is systematically lower compared to the data by about 10% for $\theta < 45°$, but the deviations become larger for higher inclinations with increasing $\theta > 45°$ because only the contribution of the flow below the dissolving slab is considered in the model, and the contribution of the top surface increases.

In order to compare the measured and calculated speeds explicitly in the case of the various candy boats, but also the salt boat, we plot U_b versus U_b^{th} in Fig. 5*C* after substituting in Eq. **8** with the relevant physical, chemical, and geometrical parameters. Except for the points corresponding to higher θ which lead to substantially lower U_b^{th}, we find that the data collapse close to the unit slope line. Thus, our model of the propulsion mechanism based on pressure difference caused by the rapidly descending density flow is consistent with our observations considering the approximations used to develop the analysis.

4. Discussions

In summary, we have demonstrated that an asymmetrically dissolving body can move rectilinearly with significant speeds while floating in a fluid. Robust directed motion is observed opposite to the principle direction in which boundary layer density currents are set up. We show that propulsion arises because of the differences in pressure fore and aft of the body due to the dense sinking current. The resulting horizontal unbalanced thrust accelerates the body till a constant velocity is reached when the thrust matches the body drag. The observed speed increases initially with the inclination angle of the body, which leads to robust generation of gravity current due to break symmetry. The speed then decreases as the horizontal projection of the gravity current decreases with an increasing angle leading to an optimal angle when the fastest speeds are observed. This observation of an efficient directed translation motion is in fact not obvious considering the relatively small mass loss rate and the intermittence of the flow. We also note that until this study, the convection flows generated by dissolution have not been quantitatively characterized, and especially, the presence of a horizontal net flow in the asymmetrical case has not been pointed out.

Even though the boundary layer is unstable and the density current is turbulent in our dissolution-driven system, the underlying propulsion mechanism at work is similar to that observed in inhomogenously heated bodies that undergo translational motion due to stable laminar buoyancy currents (17). Thus, the propulsion mechanism is observed across different systems and can be applied to far stronger density currents which result in significantly faster rectilinear speeds. In particular, we find an order of magnitude higher speeds while considering similar centimeter-scale floating bodies, with even greater speeds estimated with increasing size. Considering observations with boat pairs, one can anticipate that capillary and hydrodynamic interactions can lead to collective phenomena such as self-assembly and swarming in dissolving boat clusters.

Because shape evolution due to melting and dissolution can be similar in solids (45, 46), it is reasonable to consider whether discernible rectilinear transport can occur during melting or freezing of floating ice blocks due to temperature or salinity gradients (47, 48). It has been shown that the melting of ice shelves generates upward buoyancy driving subglacial plumes before they break into icebergs (49). Similar plumes also occur at the immersed edges of icebergs. Recent models (50) estimate the plume thickness and their velocity to be about 10 m and 0.6 m/s, respectively, for an iceberg of submerged height and width of 200 m, under typical conditions observed in the polar regions of the Earth. Similar orders of magnitudes are also obtained for plumes under ice shelves with a typical melting rate of 50 m per year (49).

While icebergs come in a wide range of sizes, their shapes below the waterline are not known in much detail (51, 52). Except for tabular icebergs, the emerged part itself is rarely symmetric due to processes which lead to their formation and deterioration (53). Recent experimental works on the melting of vertical ice columns (54) have shown that vertical walls become inclined or scalloped in relation to buoyancy-driven flows with a slope sign depending on the water bath temperature. Further, we have shown that even modest inclination leads to symmetry breaking of the boundary layer flow and directed motion. Therefore, using the corresponding values in the case of ice in place of v_p and $\delta_x \sin\theta$ in Eq. **6**, we find $F_p \approx 7.0 \times 10^3$ N. By comparison, a wind of moderate speed $U_W \sim 5$ m/s exerts on an exposed surface of area $S_a = 10 \times 200$ m^2, a force $F_W \approx \rho_{air} S_a U_W^2 \approx 5 \times 10^4$ N. This would imply a corresponding additional iceberg drift speed of approximately 2 cm/s. Thus, a typical 200-m-sized iceberg would move over its body length within about 3 hours. Such an appreciable effect should be measurable in the field by placing a couple of global positioning system devices to track the location and rotation rate of a set of icebergs, while measuring the local wind and marine currents. The subsurface iceberg shape can be obtained with ground-penetrating radar (55) or with sonar placed on autonomous submarines (56). Then, by subtracting off the contributions of wind, currents, waves, and Coriolis force (25, 26, 57, 58), it may be possible to ascertain the importance of gravity-current driven propulsion by correlating them to rapidly melting icebergs with a statistically significant number of measurements. This would establish that contribution of ice melting on its drift may be not negligible, for a typical asymmetrical iceberg with inclined immersed walls. Thus, while wind and currents can lead to significant transport of sea ice and icebergs, density currents due to salinity gradients generated by iceberg melting, may in principle contribute to their transport as well.

5. Methods

A. Boat Construction. The boats are assembled by attaching a dissolving slab (dimensions 75 mm × 40 mm × 5 mm, mass ≈ 25 g) to a hollow plastic box (dimensions 30 mm × 40 mm × 35 mm with 1.5-mm thick walls, mass 10 g) with a thin layer of silicone sealant. Candy slabs are prepared following protocols used in previous studies (22, 41) to cast an inexpensive, homogeneous, reproducible, and fast-dissolving material with a prescribed shape. Rectangular-shaped slabs are prepared by blending granulated sugar, light corn syrup, and water starting with a 8:3:2 volume ratio. The mixture is then heated up to 150°C and poured into silicone molds with rectangular cross-sections, which after cooling result in solid slabs with requisite dimensions. The plastic box is 3D-printed with polyethylene terephthalate (PET) filament with a Prusa 3D MK3S printer. Additional experiments are performed with smaller slabs with dimensions 53 mm × 27 mm × 5 mm, 37 mm × 20 mm × 5 mm, and 26 mm × 14 mm × 5 mm. The salt (NaCl) slab with dimensions 41 mm × 23 mm × 6 mm is an optical rectangle window for infrared spectroscopy obtained from Alfa Aesar.

B. Experimental Protocols. Experiments to measure speeds are performed in a rectangular 75 cm × 45 cm tank filled with distilled water to a depth of 20 cm. Initially, a boat is gently placed by hand at one end of the tank. Its motion is then recorded by a camera located above the tank, with a frame rate of 5 fps. After 180 s, the boat is taken out of the water. The boat weighs typically 3 g less

after each launch, which corresponds to the amount of mass dissolved during the experiment. Measurements are performed between three and five times for each boat at which point the decrease of the size of the candy plate ceases to be negligible, and the dissolving slab is replaced.

Data, Materials, and Software Availability. All study data are included in the article in *SI Appendix* or in Datasets S1–S10.

ACKNOWLEDGMENTS. We thank Sylvain Courrech du Pont (Université Paris Cité), Olivier Devauchelle (IPG Paris) and Ramiro Godoy-Diana (ESPCI Paris) for scientific discussions as well as Animesh Biswas (Clark University) for help in performing these experiments. This research was partially funded by the ANR grants Erodiss ANR-16-CE30-0005 and PhysErosion ANR-22-CE30-0017, and by US NSF Grant No. CBET-1805398. M.C. and M.B. acknowledge the hospitality of the Department of Physics at Clark University while the initial experiments were developed and performed.

1. M. C. Marchetti *et al*., Hydrodynamics of soft active matter. *Rev. Mod. Phys.* **85**, 1143–1189 (2013).
2. C. Brennen, H. H. Winet, Fluid mechanics of propulsion by cilia and flagella. *Annu. Rev. Fluid Mech.* **9**, 339–398 (1977).
3. E. Lauga, T. R. Powers, The hydrodynamics of swimming microorganisms. *Rep. Progr. Phys.* **72**, 096601 (2009).
4. J. Elgetti, R. G. Winkler, G. Gompper, Physics of microswimmers-single particle motion and collective behavior: A review. *Rep. Progr. Phys.* **78**, 056601 (2015).
5. A. Y. Jee, Y. K. Cho, S. Granick, T. Tlusty, Catalytic enzymes are active matter. *Proc. Natl. Acad. Sci. U.S.A.* **115**, E10812–E10821 (2018).
6. S. Dorbolo, D. Volfson, L. Tsimring, A. Kudrolli, Dynamics of a bouncing dimer. *Phys. Rev. Lett.* **95**, 044101 (2005).
7. A. Kudrolli, G. Lumay, D. Volfson, L. S. Tsimring, Swarming and swirling in self-propelled polar granular rods. *Phys. Rev. Lett.* **100**, 058001 (2008).
8. R. Golestanian, T. B. Liverpool, A. Ajdari, Propulsion of a molecular machine by asymmetric distribution of reaction products. *Phys. Rev. Lett.* **94**, 220801 (2005).
9. Z. Izri, M. N. van der Linden, S. Michelin, O. Dauchot, Self-propulsion of pure water droplets by spontaneous Marangoni-stress-driven motion. *Phys. Rev. Lett.* **113**, 248302 (2014).
10. C. C. Maass, C. Krüger, S. Herminghaus, C. Bahr, Swimming droplets. *Annu. Rev. Condens. Matter Phys.* **7**, 171–193 (2016).
11. Y. S. Ryazantsev *et al*., Thermo- and soluto-capillarity: Passive and active drops. *Adv. Colloid Interface Sci.* **247**, 52–80 (2017).
12. B. Reichert, J. B. L. Cam, A. Saint-Jalmes, G. Pucci, Self-propulsion of a volatile drop on the surface of an immiscible liquid bath. *Phys. Rev. Lett.* **127**, 144501 (2021).
13. H. Linke *et al*., Self-propelled Leidenfrost droplets. *Phys. Rev. Lett.* **96**, 154502 (2006).
14. G. Lagubeau, M. L. Merrer, C. Clanet, D. Quéré, A liquid droplet placed on a hot surface can levitate, and moreover, self-propel if the surface is textured. solids can similarly self-propel. *Nat. Phys.* **7**, 395–398 (2011).
15. A. Gauthier, C. Diddens, R. Proville, D. Lohse, D. van der Meer, Self-propulsion of inverse Leidenfrost drops on a cryogenic bath. *Proc. Natl. Acad. Sci. U.S.A.* **116**, 1174–1179 (2019).
16. M. R. Allshouse, M. F. Barad, T. Peacock, Propulsion generated by diffusion-driven flow. *Nat. Phys.* **6**, 516–519 (2010).
17. M. J. Mercier, A. M. Ardekani, M. R. Allshouse, B. Doyle, T. Peacock, Self-propulsion of immersed objects via natural convection. *Phys. Rev. Lett.* **112**, 204501 (2014).
18. T. S. Sullivan, Y. Liu, R. E. Ecke, Turbulent solutal convection and surface patterning in solid dissolution. *Phys. Rev. E* **54**, 486–495 (1996).
19. M. S. Davies Wykes, J. M. Huang, G. A. Hajjar, L. Ristroph, Self-sculpting of a dissolvable body due to gravitational convection. *Phys. Rev. Fluids* **3**, 043801 (2018).
20. J. Philippi, M. Berhanu, J. Derr, S. Courrech du Pont, Solutal convection induced by dissolution. *Phys. Rev. Fluids* **4**, 103801 (2019).
21. C. Cohen, M. Berhanu, J. Derr, S. Courrech du Pont, Buoyancy-driven dissolution of inclined blocks: Erosion rate and pattern formation. *Phys. Rev. Fluids* **5**, 053802 (2020).
22. J. M. Huang, J. Tong, M. Shelley, L. Ristroph, Ultra-sharp pinnacles sculpted by natural convective dissolution. *Proc. Natl. Acad. Sci. U.S.A.* **117**, 23339–23344 (2020).
23. S. Dorbolo *et al*., Rotation of melting ice disks due to melt fluid flow. *Phys. Rev. E* **93**, 033112 (2016).
24. A. Chamolly, E. Lauga, Stochastic dynamics of dissolving active particles. *Eur. Phys. J. E* **42**, 88 (2019).
25. D. G. Mountain, On predicting ice drift. *Cold Reg. Sci. Technol.* **1**, 273 (1980).
26. L. E. Andersson, F. Scibilia, L. Imsland, An estimation-forecast set-up for iceberg drift prediction. *Cold Reg. Sci. Technol.* **131**, 88–107 (2016).
27. D. Feltham, Sea ice rheology. *Annu. Rev. Fluid Mech.* **40**, 91–112 (2008).
28. A. Alberello *et al*., Drift of pancake ice floes in the winter Antarctic marginal ice zone during polar cyclones. *J. Geophys. Res. Oceans* **125**, e2019JC015418 (2020).
29. S. Nakata *et al*., Self-rotation of a camphor scraping on water: New insight into the old problem. *Langmuir* **13**, 4454–4458 (1997).
30. M. Nagayama, S. Nakata, Y. Doi, Y. Hayashima, A theoretical and experimental study on the unidirectional motion of a camphor disk. *Physica D* **194**, 151–165 (2004).
31. A. Biswas, J. Cruz, P. Parmananda, D. Das, First passage of an active particle in the presence of passive crowders. *Soft Matter* **16**, 6138–6144 (2020).
32. D. R. Lide, Ed., *The Handbook of Chemistry and Physics* (CRC Press, 2004).
33. D. Vella, L. Mahadevan, The "cheerios effect". *Am. J. Phys.* **73**, 817–825 (2005).
34. M. J. Dalbe, D. Cosic, M. Berhanu, A. Kudrolli, Aggregation of frictional particles due to capillary attraction. *Phys. Rev. E* **83**, 051403 (2011).
35. M. Gazzola, M. Argentina, L. Mahadevan, Scaling macroscopic aquatic locomotion. *Nat. Phys.* **10**, 758–761 (2014).
36. M. Gazzola, M. Argentina, Gait and speed selection in slender inertial swimmers. *Proc. Natl. Acad. Sci. U.S.A.* **112**, 3874–3879 (2015).
37. T. Van Buren, D. Floryan, N. Wei, A. J. Smits, Flow speed has little impact on propulsive characteristics of oscillating foils. *Phys. Rev. Fluids* **3**, 013103 (2018).
38. E. Guyon, J. P. Hulin, L. Petit, C. D. Mitescu, *Physical Hydrodynamics* (Oxford University Press, ed. 2, 2015).
39. C. E. Brennen, *An Internet Book on Fluid Dynamics* (Dankat Publishing, 2006).
40. C. E. Brennen, A review of added mass and fluid inertial forces (Tech. Rep., Naval Civil Engineering Laboratory, Port Hueneme, CA, Report CR82.010, 1982).
41. R. S. Sharma, M. Berhanu, A. Kudrolli, Alcove formation in dissolving cliffs driven by density inversion instability. *Phys. Fluids* **34**, 054118 (2022).
42. S. S. Pegler, M. S. Davies Wykes, Shaping of melting and dissolving solids under natural convection. *J. Fluid Mech.* **900**, A35 (2020).
43. S. Chandrasekhar, *Hydrodynamic and Hydromagnetic Stability* (Clarendon Press, Oxford, UK, 1961).
44. H. Schlichting, *Boundary Layer Theory* (McGraw-Hill, 1979).
45. P. Meakin, B. Jamtveit, Geological pattern formation by growth and dissolution in aqueous systems. *Proc. R. Soc. A* **466**, 659–694 (2010).
46. C. Cohen, M. Berhanu, J. Derr, S. Courrech du Pont, Erosion patterns on dissolving and melting bodies (2015 gallery of fluid motion). *Phys. Rev. Fluids* **1**, 050508 (2016).
47. R. C. Kerr, Melting driven by vigorous compositional convection. *J. Fluid Mech.* **280**, 255–285 (1994).
48. R. C. Kerr, Dissolving driven by vigorous compositional convection. *J. Fluid Mech.* **280**, 287–302 (1994).
49. I. J. Hewitt, Subglacial plumes. *Annu. Rev. Fluid Mech.* **52**, 145–169 (2020).
50. C. D. McConnochie, R. C. Kerr, The turbulent wall plume from a vertically distributed source of buoyancy. *J. Fluid Mech.* **787**, 237–253 (2016).
51. R. McKenna , "Iceberg shape characterization" in *Proceedings 18th International Conference on Port and Ocean Engineering under Arctic Conditions* (Port and Ocean Engineering under Arctic Conditions, Potsdam, NY, USA, 2005), vol. 2, pp. 555–564.
52. C. Cenedese, F. Straneo, Icebergs melting. *Annu. Rev. Fluid Mech.* **55**, 377–402 (2023).
53. Y. A. Romanov, N. A. Romanova, P. Romanov, Shape and size of Antarctic icebergs derived from ship observation data. *Antarct. Sci.* **24**, 77–87 (2012).
54. S. Weady, J. Tong, A. Zidovska, L. Ristroph, Anomalous convective flows carve pinnacles and scallops in melting ice. *Phys. Rev. Lett.* **128**, 044502 (2022).
55. P. Bohleber *et al*., Ground-penetrating radar reveals ice thickness and undisturbed englacial layers at Kilimanjaro's Northern Ice Field. *Cryosphere* **11**, 469–482 (2017).
56. M. Zhou, R. Bachmayer, B. de Young, Mapping the underside of an iceberg with a modified underwater glider. *J. Field Robot.* **36**, 1102–1117 (2019).
57. T. J. Wagner, R. W. Dell, I. Eisenman, An analytical model of iceberg drift. *J. Phys. Oceanogr.* **47**, 1605–1616 (2017).
58. A. Marchenko, N. Diansky, V. Fomin, Modeling of iceberg drift in the marginal ice zone of the Barents Sea. *Appl. Ocean Res.* **88**, 210–222 (2019).